Kinematic Modeling and Control of Variable Curvature Soft Continuum Robots

Xinjia Huang, Jiang Zou, and Guoying Gu, *Member, IEEE*

***Abstract*—The compliant structure and influence of external forces usually result in complex deformation of soft continuum robots, which makes the accurate modeling and control of the robot challenging. In this article, we present a new variable curvature kinematic modeling approach for soft continuum robots by taking the external forces into consideration, achieving both accurate motion simulation and feedforward control of the robot. To this end, the variable curvature configuration is first parameterized based on the absolute nodal coordinate formulation. Then, a kinematic model is developed to describe the mappings between the defined configuration space and the actuation space with payloads. With this model, we achieve accurate and fast motion simulation for the soft continuum robot with different payloads and input pressures within 1 ms, which is verified by a set of experiments. Finally, an inverse-model-based feedforward controller is developed for a two-section soft continuum robot. The experimental results of tracking complex trajectories verify the effectiveness of our model and control strategies. The average position error of the end effector is 2.89% of the robot length. This article can also be served as a tool to design and analyze soft continuum robots with a desired workspace.**

***Index Terms*—Absolute nodal coordinate formulation (ANCF), feedforward control, soft continuum robots, variable curvature modeling.**

I. Introduction

THE EXCELLENT features of soft continuum robots, such as elastic compliance, adaptability to the environment, and operational safety, have attracted significant attentions in the field of robotics [1]–[3]. To date, there are lot of achievements on the design of soft continuum robots, such as the cable-driven soft continuum robot [4], [5], pneumatic soft continuum robots [6], [7], or dielectric elastomer actuated soft continuum robots [8]–[10]. Due to their simple structures, light weight and easy fabrication, pneumatic soft continuum robots have shown huge potential in wide applications, such as health care, environment exploration and safe human–robot interaction [11]. However, due to the infinite degrees of freedom as well as the impacts of both actuation and external forces, it is still challenging to develop an accurate and computationally efficient kinematic model for soft continuum robots.

In order to predict and control the motion of pneumatic soft continuum robots, the widely adopted modeling approaches can be divided into two categories: constant curvature approaches and variable curvature approaches.

For the constant curvature approaches, they are based on the assumption that each section's curvature of the continuum robot is constant [12], [13]. Combining with those approaches, the motions of fiber-reinforced actuators [14], [15] and pneu-net actuators [16], [17] have been well predicted with different actuator structures and input air pressures. In addition, those approaches have also been used to develop the kinematic and dynamic models for the control of planar [18], [19] and spatial soft continuum robots [20], [21]. The constant curvature approaches can achieve a significant reduction of the kinematic model parameters, but the real curvatures of soft continuum robots in practical are usually variable, especially when the external forces are nonnegligible [22].

To overcome the limitation of constant curvature assumptions, some variable curvature modeling approaches have also been developed, which usually adopt various geometrical techniques (such as piecewise constant curvature (PCC) methods [23], [24], mode shape function (MSF) methods [25], [26], Euler spiral methods [27], and Pythagorean hodograph curve methods [28]) to approximate the variable curvature backbone shape of the robots. These approaches not only can describe the kinematics of soft continuum robots more precisely, but also can be applied to establish inverse-model-based controllers in highly variable curvature conditions. However, they mainly focus on the geometrical description, where the mappings between actuation space (input air pressures) and configuration space with different payloads are usually left out. Therefore, additional visual [29] or displacement [23], [28] sensor systems are usually required to measure and estimate the real-time experimental configuration of the continuum robots for control tasks.

Although some mechanics-based modeling approaches (such as finite-element methods (FEMs) [30], [31] or some simplified methods) have taken both the actuation and external forces into

Manuscript received August 13, 2020; revised December 13, 2020; accepted January 23, 2021. Date of publication January 28, 2021; date of current version December 15, 2021. Recommended by Technical Editor S. Foong and Senior Editor H. Qiao. This work was supported in part by the China National Key R & D Program under Grant 2019YFB1311204, in part by the National Natural Science Foundation of China under Grant 52025057, in part by the Science and Technology Commission of Shanghai Municipality under Grant 20550712100. *(Corresponding author: Guoying Gu.)*

The authors are with the Soft Robotics and Biodesign Laboratory, Robotics Institute, School of Mechanical Engineering, Shanghai Jiao Tong University, Shanghai 200240, China, and also with the State Key Laboratory of Mechanical System and Vibration, Shanghai Jiao Tong University, Shanghai 200240, China (e-mail: huangxinjia@sjtu.edu.cn; ZouJiang@sjtu.edu.cn; guguoying@sjtu.edu.cn).

This article has supplementary material provided by the authors and color versions of one or more figures available at https://doi.org/10.1109/TMECH.2021.3055339.

Digital Object Identifier 10.1109/TMECH.2021.3055339

consideration, the FEMs usually need large amount of computation and those simplified methods (including continuous [32] or discrete [33], [34] Cosserat rod approaches, Euler–Bernoulli beam approaches [35], lumped system modeling [36], [37], and geometrically exact formulation [38]) are mainly utilized for the forward simulation. In summary, it is still elusive to achieve fast simulation and efficient inverse kinematic analysis simultaneously for soft continuum robots with external forces.

In the field of dynamic analysis for flexible structures, there is a discrete modeling approach termed as absolute nodal coordinate formulation (ANCF), which generally adopts the absolute coordinates and their gradients of predefined discrete nodes to parameterize the configuration of flexible structures [39]. Owing to its advantages in computational efficiency to handle both large deformation and external forces, ANCF is usually used for the static or dynamic forward simulation of flexible beams and plates [40]. Inspired by its achievements in the modeling of the soft structure made from rubber-like material [41], we aim to utilize this method for modeling soft continuum robots. It is found in this work that the absolute-coordinate-based configuration parameterization of ANCF can also contribute to efficient inverse kinematic analysis in variable curvature conditions.

In this article, a variable curvature kinematic modeling approach based on ANCF is presented for both fast motion simulation and feedforward control of soft continuum robots, where the external forces are taken into consideration. To this end, we first parameterize the variable curvature configuration of the robot by polynomial interpolation. Afterwards, the mappings between the actuation space and the configuration space of the robot with payloads are derived from static analysis. In order to identify the parameters in the model, a two-step experimental process is designed and conducted. With the identified model parameters, our model can accurately simulate the motion of soft continuum robots with different input pressures and payloads. At last, based on the developed model, the workspace of the pneumatic soft continuum robot is analyzed and an inverse-model-based feedforward controller is further designed to achieve accurately position control. To verify the effectiveness of the control strategy, we use the robot to track complex planar trajectories (such as "SJTU") with different payload conditions. The average position error of the end effector during trajectory tracking motions is 2.89% of the robot length.

The remainder of this article is organized as follows. In Section II, the variable curvature configuration of the soft continuum robot is parameterized by ANCF. In Section III, the kinematic model is developed by analyzing the mappings between the actuation space and defined configuration space with static analysis. The identification and verification of the model are presented in Section IV. Section V describes the development of the inverse-model-based feedforward controller. Finally, Section VI concludes this article.

II. Configuration Parameterization

In general, a pneumatic soft continuum robot mainly consists of several cascaded sections that are made of pneumatic elastomer actuators, as shown in Fig. 1(a). By selectively inflating the chambers of these actuators, the soft continuum robot can achieve complex motions [see Fig. 1(b)] and accomplish desired tasks. In this article, we design and fabricate a two-section planar pneumatic soft continuum robot [as shown in Fig. 1(c)]. Each section of the robot is composed of two fiber-reinforced actuators (made from silicone rubber) and an inextensible layer between them [as shown in Fig. 2(a)]. Due to the symmetry in structure, the robot's section can generate bending motions in the plane vertical to the inextensible layer when applying different air pressures to the actuators' chambers. Connecting the robot's sections to make their motions in the same plane, the soft continuum robot can be considered as a planar system.

In order to parameterize the robot's configuration, we adopt the method of ANCF. First, the soft continuum robot is discretized into $n-1$ elements by n nodes set along the center line of the robot (as shown in Fig. 2), where the ith element represents the region between the ith node and $(i+1)$th node. In the ith

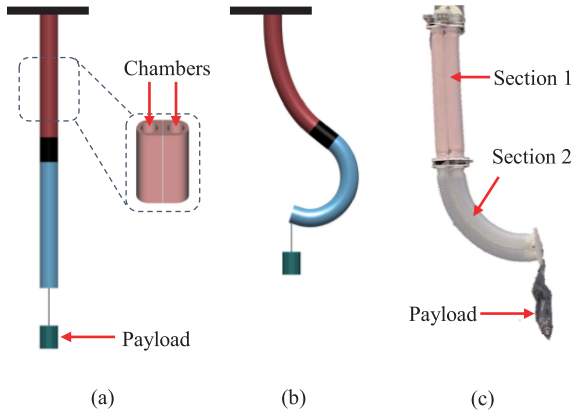

Fig. 1. Schematic illustration of the pneumatic soft continuum robot. (a) Initial state of the soft continuum robot. (b) Soft continuum robot is actuated by selectively inflating the chambers of actuators. (c) Picture of a two-section pneumatic soft continuum robot.

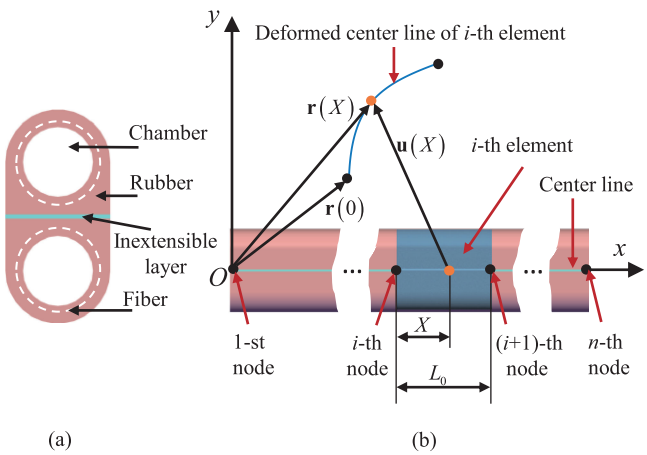

Fig. 2. Schematic illustration of the configuration description of the soft continuum robot. (a) Schematic of robot's cross section. One section of the soft continuum robot is composed of two fiber-reinforced actuators and an inextensible layer between them. (b) Variable curvature configuration of the soft continuum robot is described by $n-1$ elements.

element, an arbitrary point can be described by its arc-length parameter $X \in [0, L_0]$, where L_0 is the element length that can differ in all the elements. Thus, the position of a point after deformation can be expressed as a 2×1 vector-valued function $\mathbf{r}(X)$, with the displacement denoted as $\mathbf{u}(X)$. Typically, the positions of the two nodes of this element (the ith and $(i+1)$th node) are $\mathbf{r}(0)$ and $\mathbf{r}(L_0)$, respectively, and their absolute coordinates are defined as

$$\begin{cases} \mathbf{q}_i^{4\times1} = \left[\mathbf{r}(0)^T \ \frac{\partial \mathbf{r}^T}{\partial X}|_{X=0}\right]^T \\ \mathbf{q}_{i+1}{}^{4\times1} = \left[\mathbf{r}(L_0)^T \ \frac{\partial \mathbf{r}^T}{\partial X}|_{X=L_0}\right]^T \end{cases} \tag{1}$$

which contain the nodal positions and their gradients. Combining the absolute coordinates of the two nodes in (1) into one vector, the absolute nodal coordinates $\mathbf{q}_e$ of the ith element can be written as

$$\mathbf{q}_e{}^{8\times1} = \left[(\mathbf{q}_i)^T \ (\mathbf{q}_{i+1})^T\right]^T = [q_{e1}, q_{e2}, \ldots, q_{e8}]^T. \tag{2}$$

For each element, given its absolute nodal coordinates in (2), the cubic polynomial interpolation method can be applied to derive the expression of $\mathbf{r}(X)$ in the matrix form as follows:

$$\mathbf{r}(X) = \mathbf{S}(X)\mathbf{q}_e \tag{3}$$

where $\mathbf{S}(X)$ is a 2×8 matrix defined in (4), denoting $\mathbf{I}$ as a second-order identity matrix. Besides, s_i (i =1, 2, 3, 4) is polynomial in respect of X, which is expressed in (5)

$$\mathbf{S}(X) = \left[s_1\mathbf{I} \ s_2\mathbf{I} \ s_3\mathbf{I} \ s_4\mathbf{I}\right] \tag{4}$$

$$\begin{cases} s_1 = \frac{2X^3}{L_0{}^3} - \frac{3X^2}{L_0{}^2} + 1 \\ s_2 = \frac{X^3}{L_0{}^2} - \frac{2X^2}{L_0} + X \\ s_3 = -\frac{2X^3}{L_0{}^3} + \frac{3X^2}{L_0{}^2} \\ s_4 = \frac{X^3}{L_0{}^2} - \frac{X^2}{L_0}. \end{cases} \tag{5}$$

The element configuration represented by (3) is able to satisfy variable curvature bending and tensile deformation simultaneously. The configuration space variables of the whole robot can be defined as the absolute coordinates of all the nodes

$$\mathbf{q}^{4n\times1} = \left(\mathbf{q}_1{}^T \ \mathbf{q}_2{}^T \ \mathbf{q}_3{}^T \ \ldots \ \mathbf{q}_n{}^T\right)^T. \tag{6}$$

In this framework, the task space variable $\mathbf{x}$ is defined as the absolute coordinates of the nth node located on the base of end effector, which can be written as

$$\mathbf{x}^{4\times1} = \left[q_{4n-3} \ q_{4n-2} \ q_{4n-1} \ q_{4n}\right]^T \tag{7}$$

where q_i is the ith element of vector $\mathbf{q}$. In this sense, the positional vector $\mathbf{p}_e$ and unit axial vector η of the end effector can be given as

$$\begin{cases} \mathbf{p}_e = \left[q_{4n-3} \ q_{4n-2}\right]^T \\ \eta = \frac{1}{\sqrt{q_{4n-1}{}^2 + q_{4n}{}^2}}\left[q_{4n-1} \ q_{4n}\right]^T. \end{cases} \tag{8}$$

Hence, the task space variables in (7) are a part of the configuration space variables (6), which can make the kinematic mapping simplified.

III. Development of Kinematic Model

Based on the parameterization of the variable curvature configuration, we next develop the kinematic model of soft continuum robot to describe the mappings between the defined configuration variables $\mathbf{q}$ and actuation variables (the input air pressures) with different external forces. For this purpose, we first analyze the generalized forces of the elasticity, gravity, payload, and compressed air, respectively. Afterwards, the kinematic mappings are characterized.

A. Elasticity

The generalized elastic force can be calculated by the variation of the elastic potential energy that comes from the tensile and bending deformation of the soft sections.

The tensile deformation can be measured by the axial component of Green strain tensor [42] as

$$\bar{\varepsilon}(X) = \frac{1}{2}\left[\frac{\partial \mathbf{r}(X)^T}{\partial X}\frac{\partial \mathbf{r}(X)}{\partial X} - 1\right]. \tag{9}$$

Since there is an inextensible layer between two actuators as shown in Fig. 2(a), the value of $\bar{\varepsilon}(X)$ is small. Thus, the bending curvature can be expressed as

$$k(X) = \left\|\frac{\partial^2 \mathbf{r}(X)}{\partial X^2}\right\|. \tag{10}$$

Substituting (3) into (9) and (10), $\bar{\varepsilon}(X)$ and $k(X)$ can be calculated by

$$\begin{cases} \bar{\varepsilon}(X) = \frac{1}{2}\left[\mathbf{q}_e{}^T\frac{\partial \mathbf{S}^T(X)}{\partial X}\frac{\partial \mathbf{S}(X)}{\partial X}\mathbf{q}_e - 1\right] \\ k(X) = \left(\mathbf{q}_e{}^T\frac{\partial^2 \mathbf{S}^T(X)}{\partial X^2}\frac{\partial^2 \mathbf{S}(X)}{\partial X^2}\mathbf{q}_e\right)^{\frac{1}{2}}. \end{cases} \tag{11}$$

The total elastic potential energy in an element can be expressed as

$$U_E = \frac{1}{2}\int_0^{L_0}\left[EA\bar{\varepsilon}(X)^2 + EIk(X)^2\right]dX \tag{12}$$

where *EI* and *EA* are the flexure and elongation rigidity. We may note that the linear constitutive law is applied in (12) to improve the calculation efficiency of our model, which is reasonable for the silicon rubber like Elastosil M4601 when the stain is within 100% [43]. For practice, *EA* can be assigned with a large value to approximate the effect of inextensible layer, while *EI* can be determined by the parameter identification process that will be discussed in the Section V. Here, the variation of (12) can be expressed as

$$\delta U_E = -\left(\mathbf{Q}_E^e\right)^T\delta\mathbf{q}_e \tag{13}$$

where $\mathbf{Q}_E^e$ represents the generalized elastic force vector of the element, which can be written as

$$\mathbf{Q}_E^e = -\frac{\partial U_E}{\partial \mathbf{q}_e}. \tag{14}$$

B. Gravity

The gravity is considered as a distributed force along the robot's backbone. Defining ρ and g as the linear density of the

soft continuum robot and acceleration of gravity, respectively, the distributed force caused by the gravity can be expressed as the vector

$$\mathbf{f}(X) = \begin{bmatrix} 0 & -\rho g \end{bmatrix}^T. \tag{15}$$

The gravitational potential energy can then be expressed as

$$U_G = -\int_0^{L_0} \mathbf{f}(X)^T \mathbf{r}(X) \mathrm{d}X. \tag{16}$$

Substituting (3) into (16), the virtual work done by the gravity is

$$\delta W_G = -\delta U_G = \left(\mathbf{Q}_G^e\right)^T \delta \mathbf{q}_e \tag{17}$$

where $\mathbf{Q}_G^e$ is the generalized force of gravity that can be written as

$$\mathbf{Q}_G^e = \int_0^{L_0} \mathbf{S}(X)^T \mathbf{f}(X) \mathrm{d}X. \tag{18}$$

C. Payload

The payload on the end effector can be modeled as a concentrated force acted on the last node, which can be expressed by a 2×1 vector

$$\mathbf{F} = \begin{bmatrix} F_x & F_y \end{bmatrix}^T. \tag{19}$$

The corresponding virtual work can be obtained by

$$\delta W_L = \mathbf{F}^T \delta \mathbf{r} \,|_{X=L_0} = \left(\mathbf{Q}_F^e\right)^T \delta \mathbf{q}_e \tag{20}$$

where $\mathbf{Q}_F^e$ refers to the generalized force of external payload expressed as

$$\mathbf{Q}_F^e = \begin{pmatrix} \mathbf{0}^{1\times 4} & \mathbf{F}^T & \mathbf{0}^{1\times 2} \end{pmatrix}^T. \tag{21}$$

D. Compressed Air

Generally, the effect of compressed air can be modeled as a distributed torque $m(X)$ acted on the backbone of the robot. The work done by it on an element can be calculated as

$$W_M = \int_0^{L_0} m(X) k(X) dX. \tag{22}$$

Especially, when the robot's cross section is uniform along the backbone, the distributed torque can be simplified as a pair of concentrated actuation torques ($-M$ and M) acted on the two ends of one robot's section. Neglecting the deformation of robot's cross sections, M can be calculated by

$$M = \sum S_i P_i \tag{23}$$

where P_i is the input air pressure of the ith chamber and S_i is a coefficient depending on the chamber shape and position.

When a bending torque M caused by the compressed air is acted on a node of element ($X = 0$ or L_0), the virtual work done by it can be defined by

$$\delta W_M = \begin{cases} M \cdot \delta\theta_1 & (X = 0) \\ M \cdot \delta\theta_2 & (X = L_0) \end{cases} \tag{24}$$

where $\delta\theta_1$ and $\delta\theta_2$ refer to the virtual rotation angles of the center line at the two nodes of given element. In addition, the unit axial vector $\mathbf{n}_1$ and $\mathbf{n}_2$ can be expressed as

$$\begin{aligned} \mathbf{n}_1 &= \frac{1}{\sqrt{{q_{e3}}^2 + {q_{e4}}^2}} \begin{bmatrix} q_{e3} & q_{e4} \end{bmatrix}^T \\ \mathbf{n}_2 &= \frac{1}{\sqrt{{q_{e7}}^2 + {q_{e8}}^2}} \begin{bmatrix} q_{e7} & q_{e8} \end{bmatrix}^T \end{aligned} \tag{25}$$

where q_{ei} represents the ith element of vector $\mathbf{q}_e$.

Hence, the two virtual rotation angles can be calculated as

$$\delta\theta_1 = \mathbf{n}_1 \times \left(\frac{\partial \mathbf{n}_1}{\partial \mathbf{q}_e} \delta \mathbf{q}_e\right), \delta\theta_2 = \mathbf{n}_2 \times \left(\frac{\partial \mathbf{n}_2}{\partial \mathbf{q}_e} \delta \mathbf{q}_e\right). \tag{26}$$

Substituting (26) into (24), the virtual work can be further expressed as

$$\delta W_M = \left(\mathbf{Q}_A^e\right)^T \delta \mathbf{q}_e \tag{27}$$

where $\mathbf{Q}_A^e$ is the generalized force generated by the compressed air, which can be expressed as

$$\mathbf{Q}_A^e = \begin{cases} \begin{bmatrix} \mathbf{0}^{1\times 2} & -\frac{q_{e4}M}{{q_{e3}}^2+{q_{e4}}^2} & \frac{q_{e3}M}{{q_{e3}}^2+{q_{e4}}^2} & \mathbf{0}^{1\times 4} \end{bmatrix} & (X = 0) \\ \begin{bmatrix} \mathbf{0}^{1\times 6} & -\frac{q_{e8}M}{{q_{e7}}^2+{q_{e8}}^2} & \frac{q_{e7}M}{{q_{e7}}^2+{q_{e8}}^2} \end{bmatrix} & (X = L_0) \end{cases}. \tag{28}$$

E. Kinematic Mappings

Based on the results of (14), (18), (21), and (28), the total generalized forces $\mathbf{Q}^e$ (a 8×1 vector) acted on each element of one robot's section can be expressed as

$$\mathbf{Q}^e = \begin{cases} \mathbf{Q}_E^e + \mathbf{Q}_G^e + \mathbf{Q}_A^e & \text{the first element} \\ \mathbf{Q}_E^e + \mathbf{Q}_G^e & \text{the middle elements} \\ \mathbf{Q}_E^e + \mathbf{Q}_G^e + \mathbf{Q}_F^e + \mathbf{Q}_A^e & \text{the end element.} \end{cases} \tag{29}$$

Then, the generalized force vector $\mathbf{Q}^{4n\times 1}$ corresponding to the global configuration variables $\mathbf{q}$ can be assembled by $\mathbf{Q}^e$ according to the node number. As for a multiple-sectional soft continuum robot, the following equilibrium equations in the static condition should be satisfied:

$$\mathbf{Q}\left(\mathbf{q}, \mathbf{M}\left(\mathbf{P}\right), \mathbf{F}\right) = \mathbf{0}^{4n\times 1} \tag{30}$$

where $\mathbf{M}$ is the vector representing actuation torques generated by all the sections, and $\mathbf{P}$ is a vector of corresponding input pressures in all the sections.

In practice, one end of the soft continuum robot should be fixed on the base. This can be described in our model by introducing a set of boundary conditions for the absolute coordinates of the base node $\mathbf{q}_1$. Thus, the final equilibrium equations come into

$$\mathbf{Q}_2{}^{4n\times 1}\left(\mathbf{q}, \mathbf{M}\left(\mathbf{P}\right), \mathbf{F}\right) = \begin{bmatrix} \mathbf{q}_1 - \bar{\mathbf{q}}_1 \\ \mathbf{Q}' \end{bmatrix} = \mathbf{0}^{4n\times 1} \tag{31}$$

where $\bar{\mathbf{q}}_1$ is the fixed value of $\mathbf{q}_1$, and $\mathbf{Q}'$ is the subvector consisted by the last $4n-4$ elements of $\mathbf{Q}$.

Actually, this set of equations (31) characterizes the mappings between the configuration variables $\mathbf{q}$ and actuation variables $\mathbf{P}$ with the given payload $\mathbf{F}$, which can be used for both forward kinematic simulation and inverse kinematic analysis. For the forward simulation tasks, once $\mathbf{P}$ and $\mathbf{F}$ are given, the configuration variables $\mathbf{q}$ can be directly obtained by solving (31) with

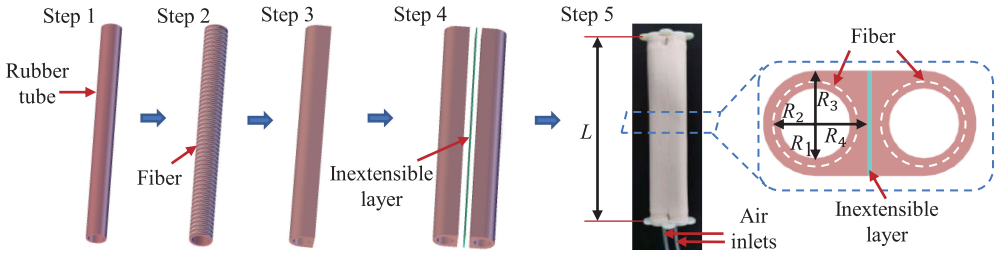

Fig. 3. Schematic illustration of the design and fabrication for one section of the soft continuum robot. Step 1: The silicone rubber tube is fabricated by molding. Step 2: Fiber is then wound along the rubber tube. Step 3: A second molding step is taken to encapsulate the actuator and form a flat face. Step 4: Two single-chamber actuators are assembled with an extensible layer between them. Step 5: Finally, one continuum robot section is sealed by two end plates, one of which reserves two ports for the flow of the air. The cross-sectional view of the fabricated robot's section is also shown.

the Newton–Raphson algorithm [44]. The inverse kinematic problems will be discussed in Section V.

Furthermore, the derivative of (31) with respect to time can be expressed as

$$\dot{\mathbf{Q}}_2 = \frac{\partial \mathbf{Q}_2}{\partial \mathbf{q}}\dot{\mathbf{q}} + \frac{\partial \mathbf{Q}_2}{\partial \mathbf{M}}\dot{\mathbf{M}} = \mathbf{0}. \tag{32}$$

Hence, the differential relationship between $\mathbf{M}$ and $\mathbf{q}$ can be given as

$$\begin{aligned} &\dot{\mathbf{q}} = \mathbf{J}_M \dot{\mathbf{M}} \\ &\text{where} \quad \mathbf{J}_M = -\left(\frac{\partial \mathbf{Q}_2}{\partial \mathbf{q}}\right)^{-1}\frac{\partial \mathbf{Q}_2}{\partial \mathbf{M}}. \end{aligned} \tag{33}$$

Combining (7) and (33), the relation between task-space velocity and actuation force velocity can be determined by

$$\dot{\mathbf{x}} = \widetilde{\mathbf{J}_M}\dot{\mathbf{M}} \tag{34}$$

where $\widetilde{\mathbf{J}_M}$ refers to the submatrix generated by the last four rows of $\mathbf{J}_M$.

IV. Parameter Identification

In our developed model, there are two sets of actuator-dependent parameters that need to be determined. The first one is the flexural rigidity EI, with the other being the coefficients S_i used for the calculation of actuation torque. In the following section, we introduce the fabrication and identification processes for the two sections of the soft continuum robot shown in Fig. 1(c).

A. Fabrication

In this article, two sections of a planar soft continuum robot with double chambers [shown in Fig. 1(c)] are designed and fabricated. As shown in Fig. 3, the fabrication processes for each section are as follows:

1) fabricate the silicone rubber tube by molding;
2) wind the fiber along the rubber tube;
3) take a second molding step to encapsulate the actuator and form a flat face;
4) assemble two actuators with an inextensible layer between them;
5) seal the fabricated robot's section by two end plates, one of which reserves two ports for the flow of the air.

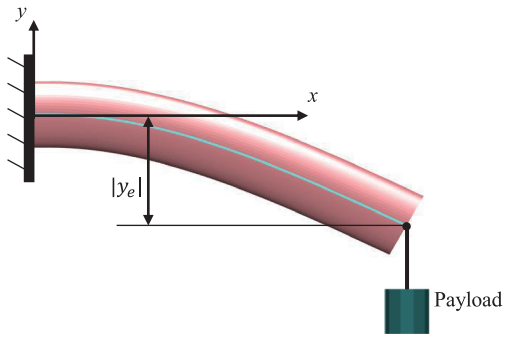

Fig. 4. Schematic diagram of static loading test for one section of the soft continuum robot.

The geometrical parameters shown in the figure are given as: $R_1 = 6$ mm, $R_2 = 7.5$ mm, $R_3 = 9$ mm, $R_4 = 9$ mm, and $L = 175$ mm. In order to prevent leakage, ribbon is wound tightly around the two ends of each robot's section. The end plates can also be used to connect additional robot's sections into a multisectional soft continuum robot. It should be noted that the kinematic model we developed can handle various materials of the actuator by the parameter identification processes. Here, we fabricate the two robot's sections with different types of silicone rubber: Elastosil M4601 (for section 1) and Dragon skin 20 (for section 2).

B. Identification of Flexural Rigidity

In order to identify the flexural rigidity of each section of the soft continuum robot, a set of static loading tests are first conducted. As shown in Fig. 4, when one robot section is fixed horizontally without actuation, the deformation of this section is generated by gravity and the payload at end. Given a value of EI, the vertical displacement of the section's end q_{4n-2} can be calculated by (31). When the actual vertical displacement is measured as y_e, an optimization model for identifying EI can be formulated as

$$\begin{aligned} &\min_{EI} \quad |q_{4n-2} - y_e| \\ &\text{subject to } \mathbf{Q}_2 = \mathbf{0}. \end{aligned} \tag{35}$$

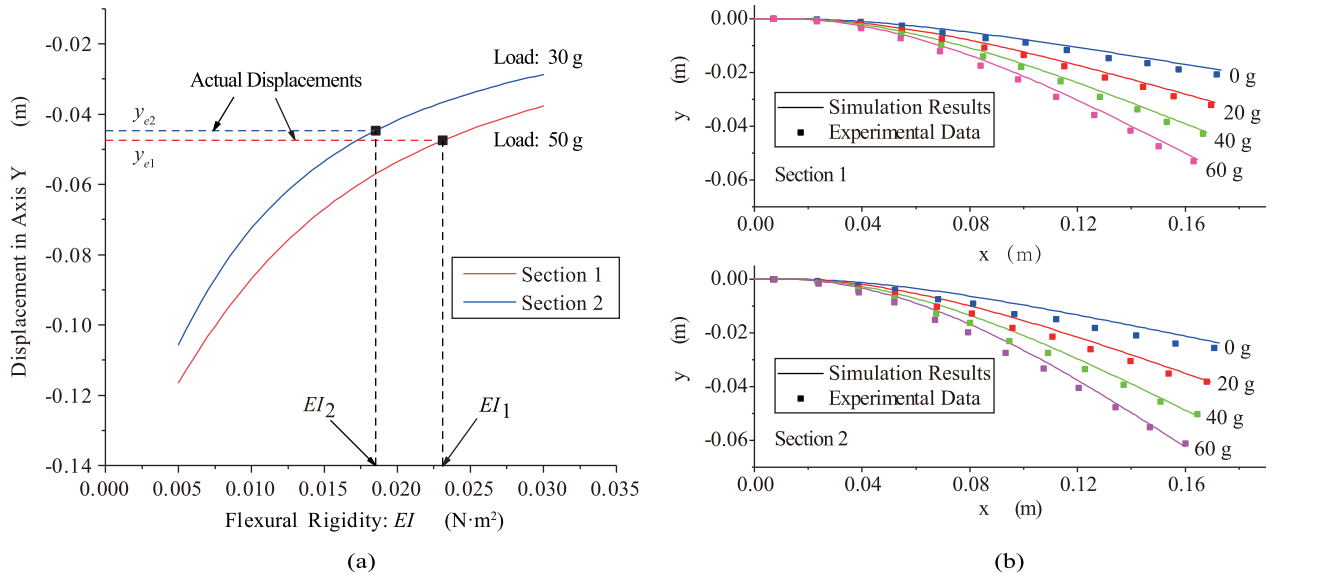

Fig. 5. Identification of flexural rigidities for two sections of the soft continuum robot. (a) Curves show the relation between the flexural rigidity and simulated vertical displacement of section's end with given payloads. (b) Identification results are applied to simulate the configuration of the two sections with different loads at their ends.

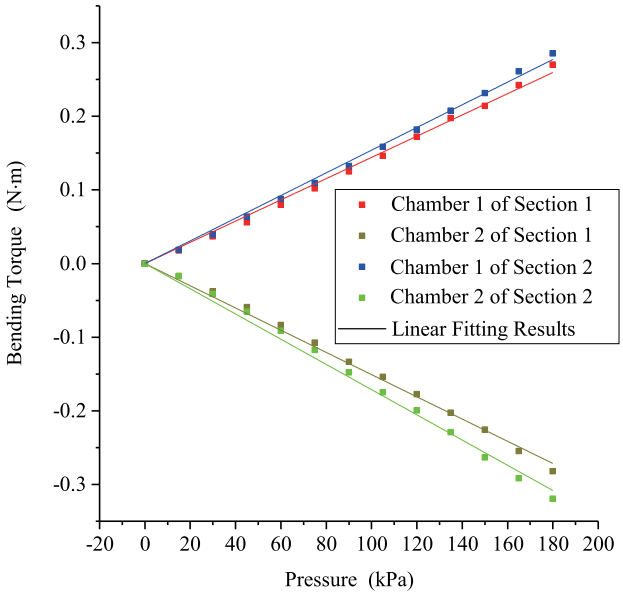

Fig. 6. Relation between bending torques and input air pressures in chambers is approximately linear.

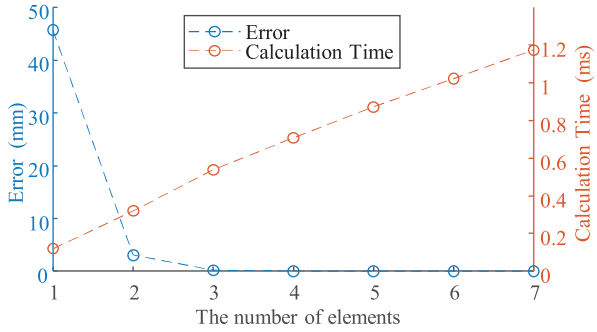

Fig. 7. Relation among the number of elements, prediction errors, and the calculation time for simulation of a one-section soft continuum robot (where the robot's length $L = 175$ mm, flexural rigidity $EI = 0.02$ N $\cdot$ m^2, and actuation torque $M = \frac{\pi EI}{2L}$).

In general, the theoretical vertical displacement q_{4n-2} should be monotonic with respect to the given EI. Hence, the optimal result of EI in (35) can be obtained by iteratively solving (31) with the bisection method.

In experiments, all the displacement data are measured by a camera system (Prime 13, OptiTrack). Loading sections 1 and 2 with 30 and 50 g weight, respectively, the actual vertical displacements of these two sections are measured as $y_{e1} = -47.4$ mm and $y_{e2} = -44.7$ mm. Fig. 5(a) shows the calculated results of the relation between q_{4n-2} and EI for the two sections by (31). The flexure rigidities of sections 1 and 2 are then determined as $EI_1 = 0.0231$ N $\cdot$ m^2 and $EI_2 = 0.0184$ N $\cdot$ m^2, respectively.

The identification results are verified by changing the magnitudes of loads, and then, comparing the simulated deformation (by EI_1 and EI_2) and the positions of markers along the two sections, as shown in Fig. 5(b). The mean errors of the vertical displacements of the end point of sections 1 and 2 are measured as 0.93 and 0.82 mm, respectively.

C. Identification of Actuation Torques

In order to identify the relationship between the actuation torque M and input air pressures, a set of horizontal bending tests are first conducted.

Considering that when one robot's section is settled in a horizontal plane, the vertical gravity will have no impact on the bending motion of it. Inflating one air chamber with input

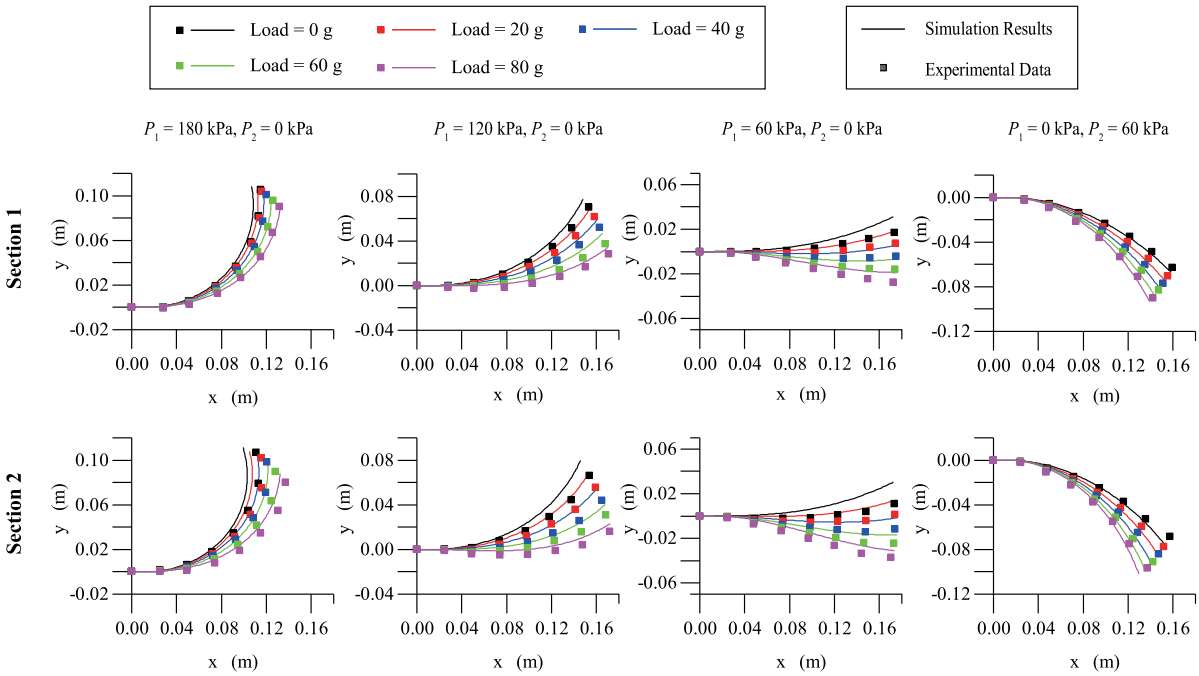

Fig. 8. Comparisons between the simulation results of the presented model and the experimental data, when maintaining the input air pressures at several given values and changing the magnitude of payloads.

pressure P, the total bending angle $\theta(P)$ of the actuator can be formulated by

$$\theta(P) = \int_0^{L_a} \frac{M(P)}{EI(X)} dX \tag{36}$$

where L_a is the flexible length of the actuator.

Taking EI as a constant that has been identified, the horizontal motion of the actuator can be simplified into a constant curvature one. In this case, (36) can be reduced into

$$M = \frac{EI\theta(P)}{L_a}. \tag{37}$$

By applying different input air pressures to each chamber of the robot's section, the resulted actuation torques are calculated with (37) by measuring the bending angle. The experimental results are shown in Fig. 6, which shows that the actuation torque M has a considerable linear relation with the input pressure. Hence, the linear fitting method is applied to obtain the value of coefficients S_i for section 1 ($S_1 = 1.23 \times 10^{-6}$ m^3 and $S_2 = -1.36 \times 10^{-6}$ m^3) and section 2 ($S_1 = 1.44 \times 10^{-6}$ m^3 and $S_2 = -1.51 \times 10^{-6}$ m^3).

D. Verification of the Identified Model

After the identification processes, the presented model can be used to simulate the robot's motion with different input pressures and payloads. We may mention that the larger number of elements can generally improve the model's accuracy, which, however, will increase the burden of calculation time. As a simplified illustration, Fig. 7 shows comparisons of calculation time and prediction errors (compared with the theoretical values) with different number of elements for a one-section soft continuum robot. From this figure, it can be observed that the prediction errors are at the same level when the number of elements is larger than four, while the calculation time is different. In the following simulation, we discrete the flexible part of each robot's section into four elements (the length of each is 3.82 cm).

To verify the model, one set of experiments is conducted by the following steps:

1) fix each section's base of the soft continuum robot in the horizontal direction;
2) inflate the chambers in the two sections with certain input pressures;
3) change the payloads at the end of each section gradually, and capture the robots' configuration;
4) change the input pressures and carry out step 3) repeatedly.

The results of this set of experiments are shown in Fig. 8. The average prediction errors of the sections' end positions are 8.94 mm and the average time cost for the calculation of the robot's motions in all the presented conditions is 0.994 ms.

Remark: We note that the observed prediction errors may be caused by several factors, including the change of robot's flexural rigidity during inflation, as well as the nonlinear relation between the actuation torque and applied pressures. The model's accuracy can be further improved by taking the nonlinear constitutive law rather than (12), and analyzing the nonlinearity of the relation between the actuation torque and applied pressures. This work mainly focuses on proposing the new variable curvature kinematic modeling approach, and the further improvement will be considered in the future study.

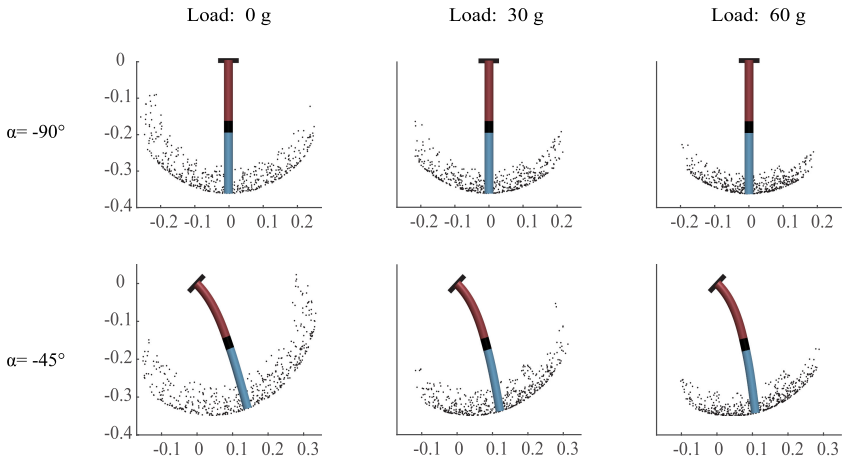

Fig. 9. Workspace analysis of the soft continuum robot with different base orientations and payloads at the end. Coordinate unit: (m).

V. Motion Control

In this section, our developed kinematic model is applied for the workspace analysis and feedforward control of the two-section soft continuum robot shown in Fig. 1(c), with the identified parameters introduced in Section IV.

A. Workspace Analysis

Due to their compliant bodies, the workspaces of soft robots not only depend on their structures but also are influenced by the payloads and base orientations.

Defining α as the orientation angle of the base, then $\bar{\mathbf{q}}_1$ in (31) can be set as

$$\bar{\mathbf{q}}_1 = \begin{bmatrix} L_e \cos\alpha & L_e \sin\alpha & \cos\alpha & \sin\alpha \end{bmatrix} \tag{38}$$

where L_e is the length of an end plate. Given the input pressures of each section of the robot, the position of the end effector can be calculated by (31). Setting the maximum input air pressure as 200 kPa, the workspaces with different loads and base orientations can be analyzed by Monte Carlo simulation. Fig. 9 shows the unactuated configurations of the robot and corresponding workspace in different conditions. The result illustrates that payloads can significantly reduce the area of the workspace, while the base orientation can influent the shape and position of it. Typically when $\alpha = -90°$, the payloads of 30 g and 60 g will result in 37.5% and 63.8% reduction of the workspace.

B. Feedforward Controller

In the developed kinematic model, we establish the mappings between the configuration variables and actuation variables with different payloads and base orientations. Here, a feedforward controller based on our model is presented.

To begin with, giving the actual payload and coordinates of the target point as $\bar{\mathbf{F}}$ and $\begin{bmatrix} \bar{q}_{4n-3} & \bar{q}_{4n-3} \end{bmatrix}^T$, (31) can be rewritten as

$$\mathbf{Q}_2(\tilde{\mathbf{h}}, \tilde{\mathbf{c}}) = \mathbf{0}^{4n\times 1}$$

$$\tilde{\mathbf{h}}^{4n\times 1} = \begin{bmatrix} \mathbf{M} & q_1 & q_2 & \dots & q_{4n-4} & q_{4n-1} & q_{4n} \end{bmatrix}^T$$

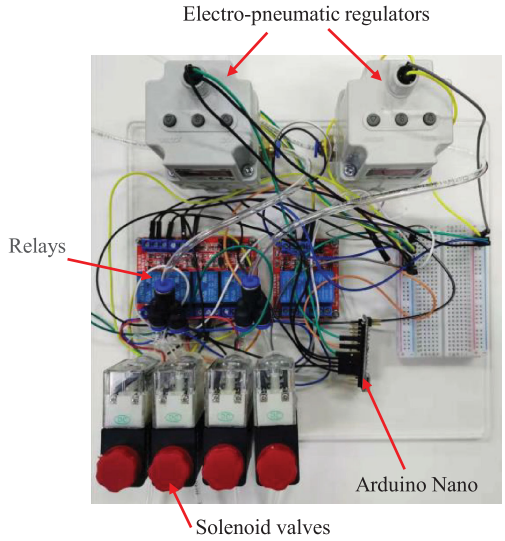

Fig. 10. Pneumatic regulation system.

$$\tilde{\mathbf{c}}^{4\times 1} = \begin{bmatrix} \bar{\mathbf{F}} & \bar{q}_{4n-3} & \bar{q}_{4n-2} \end{bmatrix}^T \tag{39}$$

where $\tilde{\mathbf{h}}$ and $\tilde{\mathbf{c}}$ are the vectors of indeterminate and determinate variables, respectively.

Based on (39), the inverse kinematic problem can be solved by the following method. First, the vector $\tilde{\mathbf{c}}$ in (39) is regarded as a generalized load, which can be divided into a series of load increments. For each increment step where $\tilde{\mathbf{c}} = \tilde{\mathbf{c}}_i$, $\tilde{\mathbf{h}}$ can be updated by a loop of the Newton–Raphson process following the iterative form as follows:

$$\tilde{\mathbf{h}}_{j+1} = \tilde{\mathbf{h}}_j - \mathbf{J}_h{}^{-1}\Big|_{\tilde{\mathbf{h}}=\tilde{\mathbf{h}}_j, \tilde{\mathbf{c}}=\tilde{\mathbf{c}}_i} \mathbf{Q}_2\left(\tilde{\mathbf{h}}_j, \tilde{\mathbf{c}}_i\right) \quad \text{where} \quad \mathbf{J}_h = \frac{\partial \mathbf{Q}_2(\tilde{\mathbf{h}}, \tilde{\mathbf{c}})}{\partial \tilde{\mathbf{h}}}. \tag{40}$$

The iterative process in each increment step should be terminated when the value of $\|\mathbf{Q}_2(\tilde{\mathbf{h}}_j, \tilde{\mathbf{c}}_i)\|$ satisfies the precision requirement. Finally, the configuration variables $\mathbf{q}$ and actuation torques $\mathbf{M}$ can be both obtained according to target points. In order to generate desired actuation toque for the ith section, one of

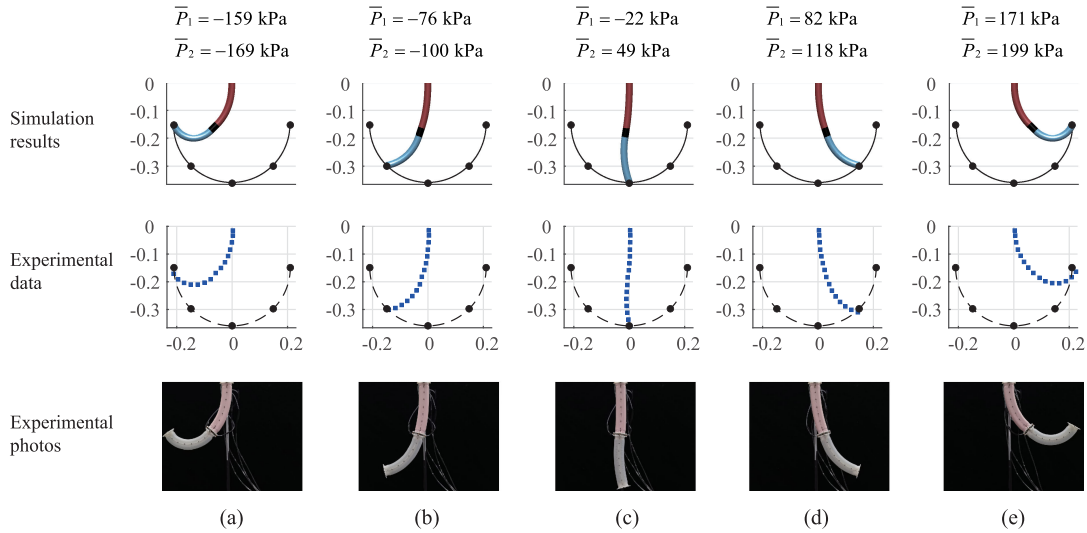

Fig. 11. Comparisons among the simulation results (the top row), markers' positions (the middle row), and the robot's pictures (the bottom row) of the point-to-point tracking test. (a) $\overline{P}_1 = -159$ kPa, $\overline{P}_2 = -169$ kPa. (b) $\overline{P}_1 = -76$ kPa, $\overline{P}_2 = -100$ kPa. (c) $\overline{P}_1 = -22$ kPa, $\overline{P}_2 = 49$ kPa. (d) $\overline{P}_1 = 82$ kPa, $\overline{P}_2 = 118$ kPa. (e) $\overline{P}_1 = 171$ kPa, $\overline{P}_2 = 199$ kPa. Coordinate unit: (m).

the chambers should be inflated with input air pressure P_i, which can be calculated by the identified model. For simplification, $\overline{P}_i$ is defined as

$$\overline{P}_i = \begin{cases} P_i, & M_i > 0 \\ -P_i, & M_i < 0 \end{cases} \tag{41}$$

which can represent the inflated chamber and input pressure simultaneously.

In order to implement the aforementioned control strategy, a pneumatic regulation system is constructed, as shown in Fig. 10. The input air pressures for the inflation of actuators are controlled by two electropneumatic regulators (ITV1050-312 L, SMC). Each pneumatic regulator is connected to two solenoid valves (2V-025-08, Delixi). They are controlled by relays to determine which chamber is under pressure regulation. All the electropneumatic regulators and relays are regulated by an Arduino Nano board interacted with MATLAB software on PC.

C. Point-to-Point Motion

With the developed feedforward controller and the pneumatic regulation system, the experiment of the point-to-point motion test is first conducted. The soft continuum robot is fixed on the base in the vertical direction, where $\alpha = -90^\circ$. Based on the analyzed workspace, five typical target points are set along a semicircle whose radius is 0.21 m. According to the positions of target points, the calculated values of input pressures are applied to the robot. Then, the real configurations of the robot are captured by the camera system (Prime 13, OptiTrack).

Fig. 11 shows the comparisons between the simulation and experimental results. It demonstrates that the robot's configuration simulated by our model can match the experimental results well, and the mean position errors of the end effector is 1.3 cm.

D. Trajectory Tracking

To further verify the control strategy, we use the soft continuum robot to track complex trajectories with payloads.

As for a desired trajectory, it can be discretized by a sequence of points $\{x_{di}, y_{di}\}$. Thus, the tracking motion can be divided into a series of point-to-point motions, which can be achieve by the control strategy we have discussed. It should be noted that, the robot can possibly reach a target point with different configurations. For the smoothness of the solutions, the initial values of $\tilde{\mathbf{h}}$ and $\tilde{\mathbf{c}}$ for solving (39) with respect to ith point should be set as the solution for the $(i-1)$th point.

In experiment, we first set the orientation angle α of the base as -90°, and the payloads are chosen as 0 and 30 g with the consideration for maintaining a relatively suitable range of the workspace, as shown in Fig. 9. Then trajectories of four letters "SJTU" are defined in the analyzed workspace, with $m = 38$ points assigned uniformly along them. Afterwards, the control efforts of equivalent pressures $\overline{P}_1$ and $\overline{P}_2$ defined in (41) for the two robot's sections are calculated for all the points, as shown in Fig. 12(a) and (d). The average time cost for the calculation of input pressures in each target point is 0.912 ms implemented by MATLAB, which allows a maximum frequency for sending the control commands around 1 kHz. Fig. 12(b) and (e) shows the comparisons between the defined trajectories and the experimental data of the marker positions at the end effector. Fig. 12(c) and (f) shows the ratio of the position error to the robot's length in each discrete point along the given trajectories, the average value of them is 2.89%. The experimental results well demonstrate the effectiveness of the model-based feedforward controller.

Remark: Compared with the existing feedback controllers, the presented feedforward controller does not require additional sensor systems for measuring the robot's real-time configuration and can work stably with different loading conditions.

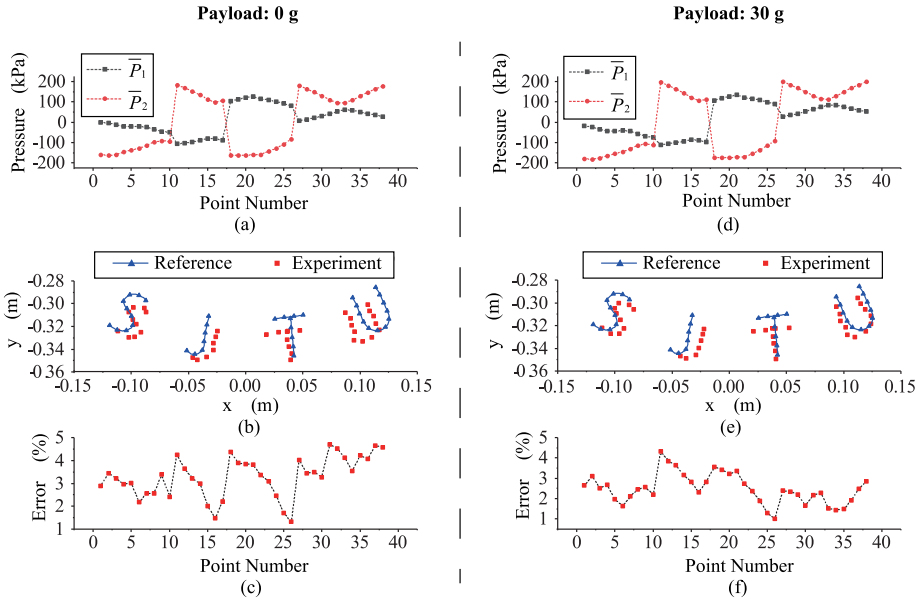

Fig. 12. Trajectory tracking results of the two-section soft continuum robot. Without payload: (a) Input air pressures for two sections; (b) comparison between desired trajectories and the actual ones captured by the vision system; and (c) position errors compared to the robot's length on each given discrete point. With a payload of 30 g: (d) Input air pressures for two sections; (e) comparison between desired trajectories and the actual ones captured by the vision system; and (f) position errors compared to the robot's length on each given discrete point.

VI. Conclusion

This article presents an ANCF-based variable curvature kinematic modeling approach for the motion simulation and feedforward control of pneumatic soft continuum robots with external forces. To this end, the configuration of the soft continuum robot is first parameterized by the absolute coordinates of several given points along the robot's backbone. Afterwards, the kinematic model is developed to describe the mappings between actuation variables and configuration variables with static analysis. Then, the static loading and horizontal bending tests are conducted to identify the model parameters. With the identified model, the motions of each robot's section are well predicted according to the input air pressures and payloads. At last, an inverse-model-based feedforward controller for a two-section soft continuum robot is developed. The comparative experimental results of point-to-point tracking tests and trajectory tracking tests verify the effectiveness of the model-based control strategy, and the average position error of the end effector is 2.89% of the robot length.

The presented model can be used to design soft continuum robots with the desired workspace and capacity under different loading conditions and be utilized to develop the feedforward controller without using additional sensor systems for measuring the robot's real-time configuration, which will be important to extend the applications of soft continuum robots for complex manipulation tasks in the known confined environment. In addition, it is feasible to extend the presented modeling approach for spatial soft continuum robots. The main difference between the modeling object for the spatial continuum robots (such as the three-chamber ones) and planar ones is the configuration parameterization. In this article, the planar soft continuum robot is used for proof-of-concept. In fact, the effectiveness of ANCF for modeling spatial structures (such as spatial flexible beams and plates [40], [41]) has been reported.

References

[1] D. Rus and M. T. Tolley, "Design, fabrication and control of soft robots," *Nature*, vol. 521, no. 7553, pp. 467–75, 2015.
[2] C. Laschi, B. Mazzolai, and M. Cianchetti, "Soft robotics: Technologies and systems pushing the boundaries of robot abilities," *Sci. Robot*, vol. 1, no. 1, 2016, Art. no. eaah3690.
[3] Z. Shen, F. Chen, X. Zhu, K.-T. Yong, and G. Gu, "Stimuli-responsive functional materials for soft robotics," *J. Mater. Chem. B*, vol. 8, pp. 8972–8991, 2020.
[4] F. Renda, M. Giorelli, M. Calisti, M. Cianchetti, and C. Laschi, "Dynamic model of a multibending soft robot arm driven by cables," *IEEE Trans. Robot.*, vol. 30, no. 5, pp. 1109–1122, Oct. 2014.
[5] F. Xu, H. Wang, K. W. S. Au, W. Chen, and Y. Miao, "Underwater dynamic modeling for a cable-driven soft robot arm," *IEEE/ASME Trans. Mechatronics*, vol. 23, no. 6, pp. 2726–2738, Dec. 2018.
[6] A. D. Marchese, R. K. Katzschmann, and D. Rus, "A recipe for soft fluidic elastomer robots," *Soft Robot.*, vol. 2, no. 1, pp. 7–25, 2015.
[7] R. F. Shepherd *et al.*, "Multigait soft robot," *Proc. Nat. Acad. Sci.*, vol. 108, no. 51, pp. 20400–20403, 2011.
[8] G. Gu, J. Zou, R. Zhao, X. Zhao, and X. Zhu, "Soft wall-climbing robots," *Sci. Robot.*, vol. 3, no. 25, 2018, Art. no. eaat2874.
[9] G. Gu, J. Zhu, L. Zhu, and X. Zhu, "A survey on dielectric elastomer actuators for soft robots," *Bioinspiration Biomimetics*, vol. 12, no. 1, 2017, Art. no. 011003.
[10] G. Gu, U. Gupta, J. Zhu, L. Zhu, and X. Zhu, "Modeling of viscoelastic electromechanical behavior in a soft dielectric elastomer actuator," *IEEE Trans. Robot.*, vol. 33, no. 5, pp. 1263–1271, Oct. 2017.
[11] C. Majidi, "Soft robotics: A. perspective-current trends and prospects for the future," *Soft Robot.*, vol. 1, no. 1, pp. 5–11, 2013.
[12] R. J. Webster III and B. A. Jones, "Design and kinematic modeling of constant curvature continuum robots: A review," *Int. J. Robot. Res.*, vol. 29, no. 13, pp. 1661–1683, 2010.
[13] M. Rolf and J. J. Steil, "Constant curvature continuum kinematics as fast approximate model for the bionic handling assistant," in *Proc. IEEE/RSJ Int. Conf. Intell. Robots Syst.*, 2012, pp. 3440–3446.

[14] F. Connolly, C. J. Walsh, and K. Bertoldi, "Automatic design of fiber-reinforced soft actuators for trajectory matching," *Proc. Nat. Acad. Sci. USA*, vol. 114, no. 1, pp. 51–56, 2017.
[15] P. Polygerinos *et al.*, "Modeling of soft fiber-reinforced bending actuators," *IEEE Trans. Robot.*, vol. 31, no. 3, pp. 778–789, Jun. 2015.
[16] G. Gu, D. Wang, L. Ge, and X. Zhu, "Analytical modeling and design of generalized pneu-net soft actuators with three-dimensional deformations," *Soft Robot.*, to be published, doi: 10.1089/soro.2020.0039.
[17] D. Drotman, M. Ishida, S. Jadhav, and M. T. Tolley, "Application-driven design of soft, 3-D printed, pneumatic actuators with bellows," *IEEE/ASME Trans. Mechatronics*, vol. 24, no. 1, pp. 78–87, Feb. 2019.
[18] A. D. Marchese, K. Komorowski, C. D. Onal, and D. Rus, "Design and control of a soft and continuously deformable 2 D robotic manipulation system," in *Proc. IEEE Int. Conf. Robot. Autom.*, 2014, pp. 2189–2196.
[19] C. Della Santina, R. K. Katzschmann, A. Biechi, and D. Rus, "Dynamic control of soft robots interacting with the environment," in *Proc. IEEE Int. Conf. Soft Robot.*, 2018, pp. 46–53.
[20] V. Falkenhahn, A. Hildebrandt, R. Neumann, and O. Sawodny, "Model-based feedforward position control of constant curvature continuum robots using feedback linearization," in *Proc. IEEE Int. Conf. Robot. Autom.*, 2015, pp. 762–767.
[21] V. Falkenhahn, A. Hildebrandt, R. Neumann, and O. Sawodny, "Dynamic control of the bionic handling assistant," *IEEE/ASME Trans. Mechatronics*, vol. 22, no. 1, pp. 6–17, Feb. 2017.
[22] Y. Shapiro, A. Wolf, and K. Gabor, "Bi-bellows: Pneumatic bending actuator," *Sensors Actuators A, Phys.*, vol. 167, no. 2, pp. 484–494, 2011.
[23] T. Mahl, A. Hildebrandt, and O. Sawodny, "A variable curvature continuum kinematics for kinematic control of the bionic handling assistant," *IEEE Trans. Robot.*, vol. 30, no. 4, pp. 935–949, Aug. 2014.
[24] H. Wang, B. Yang, Y. Liu, W. Chen, X. Liang, and R. Pfeifer, "Visual servoing of soft robot manipulator in constrained environments with an adaptive controller," *IEEE/ASME Trans. Mechatronics*, vol. 22, no. 1, pp. 41–50, Feb. 2017.
[25] I. S. Godage, E. Guglielmino, D. T. Branson, G. A. Medrano-Cerda, and D. G. Caldwell, "Novel modal approach for kinematics of multisection continuum arms," in *Proc. IEEE/RSJ Int. Conf. Intell. Robots Syst.*, 2011, pp. 1093–1098.
[26] I. S. Godage, G. A. Medranocerda, D. T. Branson, E. Guglielmino, and D. G. Caldwell, "Modal kinematics for multisection continuum arms," *Bioinspiration Biomimetics*, vol. 10, no. 3, pp. 035002–035002, 2015.
[27] P. S. Gonthina, A. D. Kapadia, I. S. Godage, and I. D. Walker, "Modeling variable curvature parallel continuum robots using euler curves," in *Proc. Int. Conf. Robot. Autom.*, 2019, pp. 1679–1685.
[28] I. Singh, Y. Amara, A. Melingui, P. Mani Pathak, and R. Merzouki, "Modeling of continuum manipulators using pythagorean hodograph curves," *Soft Robot*, vol. 5, no. 4, pp. 425–442, 2018.
[29] A. D. Marchese and D. Rus, "Design, kinematics, and control of a soft spatial fluidic elastomer manipulator," *Int. J. Robot. Res.*, vol. 35, no. 7, pp. 840–869, 2015.
[30] T. M. Bieze, F. Largilliere, A. Kruszewski, Z. Zhang, R. Merzouki, and C. Duriez, "Finite element method-based kinematics and closed-loop control of soft, continuum manipulators," *Soft Robot*, vol. 5, no. 3, pp. 348–364, 2018.
[31] G. Fang, C. Matte, R. B. N. Scharff, T. Kwok, and C. C. L. Wang, "Kinematics of soft robots by geometric computing," *IEEE Trans. Robot.*, vol. 36, no. 4, pp. 1272–1286, Aug. 2020.
[32] K. M. de Payrebrune and O. M. O'Reilly, "On the development of rod-based models for pneumatically actuated soft robot arms: A five-parameter constitutive relation," *Int. J. Solids Struct.*, vol. 120, pp. 226–235, 2017.
[33] F. Renda, F. Boyer, J. Dias, and L. Seneviratne, "Discrete Cosserat approach for multisection soft manipulator dynamics," *IEEE Trans. Robot.*, vol. 34, no. 6, pp. 1518–1533, Dec. 2018.
[34] S. M. H. Sadati, S. E. Naghibi, I. D. Walker, K. Althoefer, and T. Nanayakkara, "Control space reduction and real-time accurate modeling of continuum manipulators using Ritz and Ritz-Galerkin methods," *IEEE Robot. Autom. Lett.*, vol. 3, no. 1, pp. 328–335, Jan. 2018.
[35] K. Oliver-Butler, J. Till, and C. Rucker, "Continuum robot stiffness under external loads and prescribed tendon displacements," *IEEE Trans. Robot.*, vol. 35, no. 2, pp. 403–419, Apr. 2019.
[36] I. S. Godage, R. Wirz, I. D. Walker, and R. J. Webster, "Accurate and efficient dynamics for variable-length continuum arms: A center of gravity approach," *Soft Robot.*, vol. 2, no. 3, pp. 96–106, 2015.
[37] S. Sadati *et al.*, "Reduced order vs. discretized lumped system models with absolute and relative states for continuum manipulators," in *Proc. Robot. Sci. Syst. Conf.*, 2019, Art. no. 10.
[38] S. Grazioso, G. Di Gironimo, and B. Siciliano, "A geometrically exact model for soft continuum robots: The finite element deformation space formulation," *Soft Robot.*, vol. 6, no. 6, pp. 790–811, 2019.
[39] A. A. Shabana and R. Y. Yakoub, "Three dimensional absolute nodal coordinate formulation for beam elements: Theory," *J. Mech. Des.*, vol. 123, no. 4, pp. 606–613, 2000.
[40] J. Gerstmayr, H. Sugiyama, and A. Mikkola, "Review on the absolute nodal coordinate formulation for large deformation analysis of multibody systems," *J. Comput. Nonlinear Dyn.*, vol. 8, no. 3, 2013, Art. no. 031016.
[41] S. P. Jung, T. W. Park, and W. S. Chung, "Dynamic analysis of rubber-like material using absolute nodal coordinate formulation based on the non-linear constitutive law," *Nonlinear Dyn.*, vol. 63, no. 1, pp. 149–157, 2011.
[42] Y. Fung, P. Tong, and X. Chen, *Classical And Computational Solid Mechanics (Second Edition). (Advanced Series In Engineering Science)*. Singapore: World Scientific, 2017.
[43] G. Alici, T. Canty, R. Mutlu, W. Hu, and V. Sencadas, "Modeling and experimental evaluation of bending behavior of soft pneumatic actuators made of discrete actuation chambers," *Soft Robot*, vol. 5, no. 1, pp. 24–35, 2018.
[44] J. Bonet and R. Wood, *Nonlinear Continuum Mechanics for Finite Element Analysis*. Cambridge, U.K.: Cambridge Univ. Press, 2008.

Xinjia Huang (Member, IEEE) received the B.E. degree (with honors) in engineering mechanics from Chongqing University, Chongqing, China, in 2018. He is currently working toward the Ph.D. degree in mechanical engineering with Shanghai Jiao Tong University, Shanghai, China.

His research interests include design, modeling, and control of soft robotics.

Jiang Zou (Member, IEEE) received the Ph.D. degree (with honors) in mechatronic engineering from Shanghai Jiao Tong University, Shanghai, China, in 2019.

Supported by Shanghai Postdoctoral Excellence Program, he is a Postdoctor with Shanghai Jiao Tong University. His research interests include design, modeling, and control of soft robots.

Guoying Gu (Member, IEEE) received the B.E. degree (with honors) in electronic science and technology, and the Ph.D. degree (with honors) in mechatronic engineering from Shanghai Jiao Tong University, Shanghai, China, in 2006 and 2012, respectively.

Since October 2012, he has been working with Shanghai Jiao Tong University, where he is currently a Professor with the School of Mechanical Engineering. He was a Humboldt Fellow with the University of Oldenburg, Oldenburg, Germany. He was a Visiting Scholar with the Massachusetts Institute of Technology, National University of Singapore, and Concordia University. His research interests include soft robotics, bioinspired and wearable robots, smart materials sensing, actuation, and motion control. He is the author or co-author of more than 90 publications, which have appeared in *Science Robotics*, *Science Advances*, IEEE/ASME Transactions, *Advanced Functional Materials*, *Soft Robotics*, etc., as book chapters and in conference proceedings.

Dr. Gu was the Recipient of the National Science Fund for Distinguished Young Scholars, in 2020. He is currently serving as an Associate Editor for the IEEE TRANSACTIONS ON ROBOTICS and IEEE ROBOTICS AND AUTOMATION LETTERS. He has also served for several journals as the Editorial Board Member, Topic Editor, or Guest Editor, and several international conferences/symposiums as the Chair, Co-Chair, Associate Editor, or Program Committee Member.